ACS Sustainable Chemistry & Engineering

Research Article

Cite This: ACS Sustainable Chem. Eng. 2017, 5, 11086-11095

pubs.acs.org/journal/ascecg

Ammonia Mediated One-Step Synthesis of Three-Dimensional Porous Pt_xCu_{100-x} Nanochain Networks with Enhanced Electrocatalytic Activity toward Polyhydric Alcohol Oxidation

Dian Li, Kai Cai, Long Wu, Yunpeng Zuo, Wenmin Yin, Huan Zhang, Zhicheng Lu, Guilin Zhu, and Heyou Han*

State Key Laboratory of Agricultural Microbiology, College of Science, Huazhong Agricultural University, No.1, Shizishan Street, Hongshan District, Wuhan 430070, China

Supporting Information

ABSTRACT: Owing to the excellent molecular accessibility and self-supported architectures, three-dimensional (3D) porous nanostructures can promote the catalytic property of Pt-based catalysts. In this work, by using ammonia as the structure-director in the synthetic process, a facile method was developed to synthesize bimetallic 3D porous Pt_xCu_{100-x} nanochain networks (3D p-Pt_xCu_{100-x} NCNs) with tunable compositions. The 3D p-$Pt_{46}Cu_{54}$ NCNs achieve a mass activity of 8.38 A mg_{Pt}^{-1} for ethylene glycol oxidation reaction (EGOR) and 4.01 A mg_{Pt}^{-1} for glycerol oxidation reaction (GOR) in alkaline solution, which is 3.58-fold and 4.01-fold that of commercial Pt/C, respectively. The result demonstrated that the bimetallic 3D nanochain network structures facilitated the effective utilization of Pt. The ammonia mediated one-step synthetic strategy has the potential to prepare other promising 3D porous Pt-based nanomaterials in electrocatalytic applications.

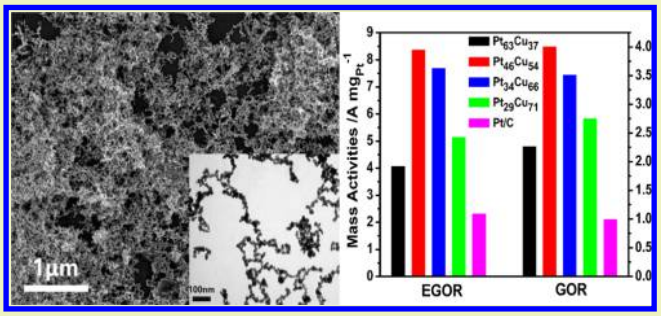

KEYWORDS: *PtCu alloys, 3D porous networks, ethylene glycol oxidations, glycerol oxidations*

INTRODUCTION

Seeking renewable resources to solve the dilemma of traditional fossil fuel shortage is a major challenge worldwide.[1] In recent decades, direct fuel cells (DFCs) have obtained extensive interest because of their special characteristics, such as high efficiency and cleanness.[2,3] Compared with conventional small molecule fuels such as methanol and ethanol, polyhydric alcohols, for instance, ethylene glycol (EG) and glycerol, exhibit particular characteristics including higher boiling points and energy density, as well as less toxicity and volatility.[4−9]

For a long time, high-performance catalysts for anodic reactions have been pursued in order to make continuous progress in fuel cell technologies.[10,11] Since there is high catalytic activity, a platinum (Pt)-based nanocrystal has been widely studied in recent years.[12,13] However, there are still several problems in the large-scale commercial application of Pt-based fuel cells. First, in view of the scarce resource and increasing cost of Pt, it is imperative to minimize the consumption of Pt.[14,15] Second, enhancing the electrocatalytic property of Pt-based electrocatalysts is another key issue for the development of fuel cells.[15,16] According to some research findings, Pt sintering, carbon corrosion, and dissolution of Pt in catalytic process can cause poorer catalytic activity, which leads to a decline in the performance of fuel cells.[17−19] Third, Pt-based catalysts are sensitive to CO-like carbonaceous intermediates which could destroy the activity and durability of the nanocatalysts.[20,21] Therefore, it is of great importance and urgency to minimize the cost and optimize the electrocatalytic property of Pt-based catalysts.

The activity and stability of nanocatalysts have close connections with their morphologies.[22,23] Therefore, considerable research efforts have been devoted to obtaining Pt-based nanoparticles with different morphologies such as core/shell nanostructures,[24] nanodendrites,[25] nanosheets,[26] hollow nanoparticles,[27] nanowires,[28−30] and nanoframes.[31−34] Despite this, the researchers keep on pursuing Pt-based bimetallic nanomaterials with novel morphology and excellent performance. The recent irruptive studies on three-dimensional (3D) porous metal nanostructures have sparked new interests toward various assembled architectures with fine-tuned building blocks.[35−37] This nanostructure owns large surface area and can offer abundant active sites via its high porosity, which efficiently improves the surface mass transport and gas diffusion. Consequently, this kind of catalyst could exhibit excellent electrocatalytical performance.[21,35,36] In addition, as self-supported catalysts, they possess intensive durability as the carbon support-corrosion is eliminated.[17,21,38] Hence, it is

Received: August 31, 2017
Revised: October 9, 2017
Published: October 9, 2017

DOI: 10.1021/acssuschemeng.7b03047
ACS Sustainable Chem. Eng. 2017, 5, 11086−11095

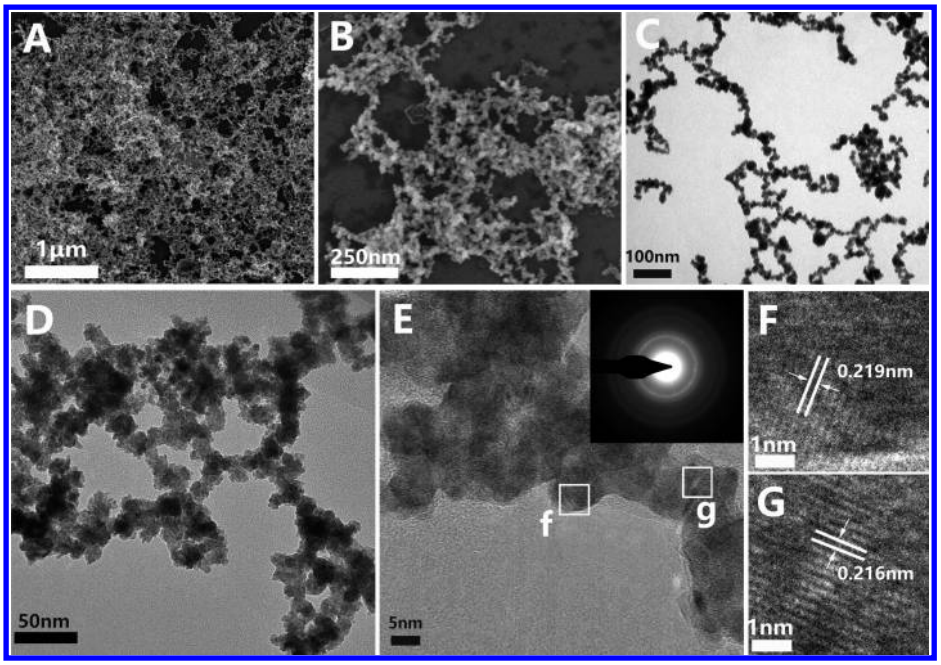

Figure 1. (A) SEM, (B) high-magnification SEM, (C, D) TEM, and (E–G) HRTEM images of as-prepared 3D p-$Pt_{46}Cu_{54}$ NCNs. Inset shows the corresponding SAED pattern.

attractive and promising to design unique 3D porous Pt-based nanocatalysts with enhanced electrocatalytic activity.

In recent years, synthesis of Pt-based bimetallic nanomaterials with relatively inexpensive metals has been extensively studied, which can not only lessen the utilization of Pt but also enhance the performance of the catalysts.[39−41] After the introduction of another metal in Pt, the lattice strain occurs due to the lattice mismatch between Pt and the second metals, which could impair chemisorption between Pt atoms and oxygenated chemicals and expose more active sites accordingly.[21,42] Moreover, the variational electronic structure of platinum with another metal may boost the improvement of the catalytic activity of Pt-based alloys.[26,29] In the context, a wide range of bimetallic nanocatalysts such as PtPd,[4,25,27] PtAg,[41] PtAu,[43−45] PtNi,[13,31,46] PtCo,[28,47,48] PtFe,[30] and PtCu[33,34,39] with enhanced catalytic activity have been synthesized. Owing to the preeminent performance, PtCu nanomaterials with different morphologies have obtained extensive research.[29,32,40] Nonetheless, the study of bimetallic PtCu nanomaterials with 3D porous nanostructure is still rare.

In this study, a straightforward one-pot strategy was proposed to prepare bimetallic alloyed 3D porous Pt_xCu_{100-x} nanochain networks (3D p-Pt_xCu_{100-x} NCNs) in aqueous solution. Ammonia acted as a structure-directing agent in the synthetic process without the addition of any surfactant. By adjustment of the ratio, four catalysts with different components were obtained, which were defined as $Pt_{63}Cu_{37}$, $Pt_{46}Cu_{54}$, $Pt_{34}Cu_{66}$, and $Pt_{29}Cu_{71}$, respectively. The electrocatalytic performances of the 3D p-Pt_xCu_{100-x} NCNs were investigated by using ethylene glycol oxidation reaction (EGOR) and glycerol oxidation reaction (GOR). As a result, they presented remarkable enhancement of electrocatalytic activity and stability for both EGOR and GOR, showing great potential in catalytic applications.

EXPERIMENTAL SECTION

Reagents and Materials. Chloroplatinic acid hexahydrate ($H_2PtCl_6·6H_2O$, AR), copper(II) nitrate trihydrate ($Cu(NO_3)_2·3H_2O$, AR), hydrazine hydrate ($N_2H_4·H_2O$, 85%, AR), ammonium hydroxide ($NH_3·H_2O$, 25%–28%, AR), sulfuric acid (H_2SO_4, AR), sodium hydroxide (NaOH, AR), ethylene glycol (EG, AR), and glycerol (AR) were purchased from the Sinopharm Chemical Reagent Co., Ltd. Nafion perfluorinated resin solution (5 wt % in mixture of lower aliphatic alcohols and water, containing 45% water) was provided by Sigma-Aldrich. Commercial platinum/carbon (Pt/C, Pt loading 20 wt % on carbon black) was obtained from Alfa Aesar (China) Chemicals Co., Ltd. All chemicals were utilized directly without further purification.

Synthesis of 3D p-Pt_xCu_{100-x} NCNs. For the typical synthesis of 3D p-$Pt_{46}Cu_{54}$ NCNs, 100 μL of H_2PtCl_6 (19.3 mM) and 100 μL of $Cu(NO_3)_2$ (20 mM) were put into 5.6 mL ultrapure water simultaneously in an ice bath. After stirring, 150 μL of ammonium hydroxide diluted 10 times was added into the mixed solution. Subsequently, 50 μL of $N_2H_4·H_2O$ (85%) was quickly dripped into the solution. The reaction system turned black rapidly, and the reaction time was controlled at about 10 min. The final products were washed twice with water and gathered by centrifugation for further characterization. The same procedure was used to synthesize 3D p-$Pt_{63}Cu_{37}$, 3D p-$Pt_{34}Cu_{66}$, and 3D p-$Pt_{29}Cu_{71}$ NCNs by adjustment of the addition amount of metal precursors (Table S1). The last acquired materials were dispersed into 0.5 mL water and sonicated to obtain well-dispersed solution.

Characterization. Scanning electron microscopy (SEM) images and high-magnification SEM images were acquired on a SU8010 field emission scanning electron microscope. Low-magnification transmission electron microscopy (TEM) images were obtained on a JEM-2100F high-resolution transmission electron microscope. High-resolution transmission electron microscopy (HRTEM) images, energy-dispersive X-ray spectroscopy (EDS) analyses, and high-angle annular dark field-scanning transmission electron microscopy (HAADF-STEM) measurements were performed with a FEI-Tecnai G2 F30 transmission electron microscope at an accelerating voltage of 200 kV. The precise composition of 3D p-Pt_xCu_{100-x} NCNs were ascertained by a PerkinElmer NexION 300Q inductively coupled plasma mass spectrometry (ICP-MS). The X-ray diffraction (XRD) spectrum was acquired by a Bruker D8 Advance X-ray diffractometer

DOI: 10.1021/acssuschemeng.7b03047
ACS Sustainable Chem. Eng. 2017, 5, 11086−11095

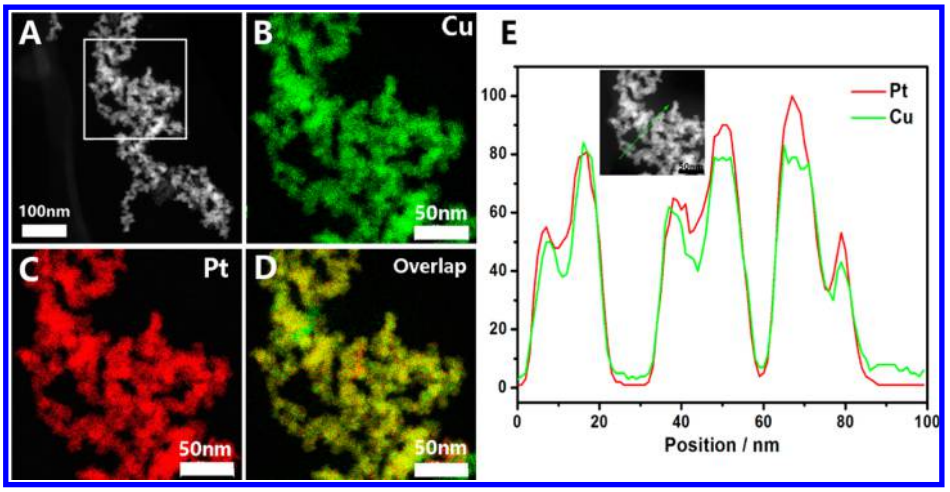

Figure 2. (A) HAADF-STEM image of 3D p-$Pt_{46}Cu_{54}$ NCNs. The elemental mapping images of (B) Cu, (C) Pt, and their (D) overlapping image. (E) Cross-sectional compositional line profiles of 3D p-$Pt_{46}Cu_{54}$ NCNs.

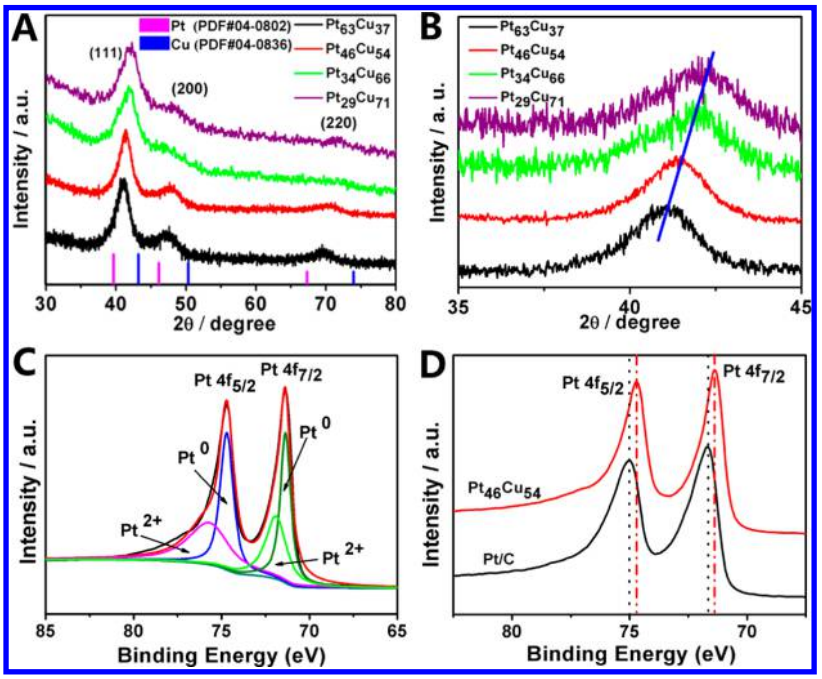

Figure 3. (A) XRD patterns of as-prepared 3D p-Pt_xCu_{100-x} NCNs: $Pt_{63}Cu_{37}$, $Pt_{46}Cu_{54}$, $Pt_{34}Cu_{66}$, and $Pt_{29}Cu_{71}$. Magenta and blue vertical lines represent the locations of Pt (PDF 04-0802) and Cu (PDF 04-0836), respectively. (B) Amplificatory view of XRD spectra. (C) High-resolution XPS spectrum of Pt 4f in 3D p-$Pt_{46}Cu_{54}$ NCNs. (D) Pt 4f XPS spectra of 3D p-$Pt_{46}Cu_{54}$ NCNs and commercial Pt/C.

with Cu Kα radiation. The X-ray photoelectron spectra (XPS) analysis was taken on a Thermo Fisher ESCALAB 250Xi spectrophotometer with Al Kα X-ray radiation and calibrated by using the C 1s peak (284.6 eV).

Electrochemical Measurements. Cyclic voltammetry (CV) and chronoamperometry experiments were carried out using a CHI 660E electrochemical workstation (Chenhua Instruments Corp, Shanghai, China). All electrochemical reactions proceeded in a conventional three-electrode cell which was composed of modified glassy carbon electrode (GCE, working electrode, diameter = 3 mm), platinum wire counter electrode, and Ag/AgCl (saturated KCl) reference electrode. Before modification, GCE was burnished carefully with 1.0, 0.3, and 0.05 μm alumina powder in succession to obtain a smooth surface, and then washed by sonication in 50% nitric acid aqueous solution. After that, 5 μL of sample solution or commercial Pt/C solution was dripped on the GCE surface by using a pipet and dried under ambient conditions. After that, the loading mass of Pt was determined by ICP-MS. Finally, the surface of GCE was covered with 4.0 μL of Nafion (0.5 wt %) and dried carefully before electrochemical tests. The modified GCE was activated electrochemically in 0.5 M H_2SO_4 before testing. EGOR and GOR measurements were carried out in a solution of 0.5 M NaOH including 0.5 M ethylene glycol or glycerol.

RESULTS AND DISCUSSION

The morphologies of prepared nanomaterials were first characterized by scanning electron microscopy (SEM). Figure 1A reveals that synthesized nanomaterials have porous spongelike morphology. Moreover, as shown in a high-magnification SEM image (Figure 1B) and transmission electron microscopy (TEM) images (Figure 1C,D), numerous interconnected nanochains exist in the whole structure. The fusions between the contiguous nanochains give rise to the formation of PtCu nanochain networks.

DOI: 10.1021/acssuschemeng.7b03047
ACS Sustainable Chem. Eng. 2017, 5, 11086−11095

The as-prepared 3D porous PtCu nanochain networks (3D p-PtCu NCNs) were further characterized by HRTEM; Figure 1E also verifies that the junctions of PtCu nanochains are fused together. The energy-dispersive X-ray spectroscopy (EDS) analysis was executed on a molybdenum carrier; Figure S1 shows that there are only elements Pt and Cu in the nanomaterials. As shown in Figure 1E, inset, the polycrystalline structure of 3D p-PtCu NCNs was demonstrated by the selected area electron diffraction (SAED) pattern. Furthermore, HRTEM images show that the lattice fringes are, respectively, with the lattice spacing distance of 0.219 nm (Figure 1F) and 0.216 nm (Figure 1G). These lattice spacings belong to the (111) planes of the face centered cubic (fcc) PtCu alloy.[29,49] The result indicates that the as-prepared nanoparticles grow along the (111) directions preferentially. The as-prepared 3D p-PtCu NCNs were also characterized by HAADF-STEM; homogeneous distributions of Pt and Cu atoms within the whole nanostructure were verified by the elemental mapping images (Figure 2A−D) and line scanning curve (Figure 2E), further reflecting the alloyed feature of 3D p-PtCu NCNs.

By adjustment of the precursors ratios in the synthesis, four kinds of the 3D p-Pt_xCu_{100-x} NCNs were obtained. The SEM, high-magnification SEM, and TEM images of other three types of 3D p-Pt_xCu_{100-x} NCNs are shown in Figure S2. The results reveal that all the nanomaterials have similar 3D porous morphology, confirming the universality of this method in synthesizing 3D nanostructures. The precise composition of the 3D p-Pt_xCu_{100-x} NCNs was measured by ICP-MS; the mole ratios of Pt to Cu were 63:37, 46:54, 34:66, and 29:71, respectively.

Figure 3A displays the XRD patterns of 3D p-Pt_xCu_{100-x} NCNs. As depicted, all of the 3D porous networks exhibit diffraction peaks at (111), (200), and (220) planes, corresponding to the typical fcc structure. The diffraction peaks from the (111) planes are more prominent than the other peaks, further reflecting that the 3D p-Pt_xCu_{100-x} NCNs grow along the (111) directions preferentially. The consequence is in accordance with the HRTEM results. The diffraction peaks of the 3D p-Pt_xCu_{100-x} NCNs are all situated between those of pure Pt (PDF 04-0802) and Cu (PDF 04-0836), which further demonstrates their alloyed structure.[4,43,44] Figure 3B displays the amplificatory view of the diffraction peaks of (111) planes, in which positive shifts take place as the quantity of Cu increases. XPS can be used for analyzing the valence states and surface compositions of nanocrystals effectively. Figure S3A shows XPS spectra of 3D p-$Pt_{46}Cu_{54}$ NCNs, where the peaks of Pt and Cu can be obviously recognized. Figure 3C exhibits the high-resolution Pt 4f XPS spectrum of 3D p-$Pt_{46}Cu_{54}$ NCNs, which shows two distinct peaks at binding energies of 74.68 and 71.38 eV, assigned to Pt $4f_{5/2}$ and Pt $4f_{7/2}$, respectively.[32,50] The two peaks are all divided into two peaks subsequently to verify the existence of Pt^0 and Pt^{2+}. According to the peak intensity, Pt^0 is the major ingredient in 3D p-$Pt_{46}Cu_{54}$ NCNs. Figure S3B exhibits the high-resolution Cu 2p XPS spectrum of 3D p-$Pt_{46}Cu_{54}$ NCNs; the Cu 2p XPS spectrum shows two distinct peaks at binding energies of 952.23 and 932.43 eV, assigned to Cu $2p_{1/2}$ and Cu $2p_{3/2}$, respectively.[32,50] Thus, there is the same conclusion that the dominant composition in 3D p-$Pt_{46}Cu_{54}$ NCNs is Cu^0. The dominant Pt^0 and Cu^0 indicate the effective reduction of the two precursors. Figure 3D shows the Pt 4f XPS spectra of 3D p-$Pt_{46}Cu_{54}$ NCNs and that of Pt/C. The peaks at binding energy of 75.03 and 71.68 eV correspond to the Pt $4f_{5/2}$ and $4f_{7/2}$ states for Pt/C, respectively. The Pt $4f_{5/2}$ binding energy of the 3D p-$Pt_{46}Cu_{54}$ NCNs (74.68 eV) is about 0.35 eV under that of commercial Pt/C, while the $4f_{7/2}$ binding energy of the 3D p-$Pt_{46}Cu_{54}$ NCNs (71.38 eV) is about 0.3 eV under that of commercial Pt/C. The remarkable change of electronic structure of Pt in 3D p-PtCu NCNs may affect their catalytic properties.[4,5]

For further investigation of the synthesis mechanism of 3D p-PtCu NCNs, a suite of control experiments were performed. In the absence of ammonia, the nanomaterials are agglomerated seriously (Figure S4A). Without addition of any capping agents, the adhesion may happen between the adjacent nanoparticles with bare crystal planes, thus leading to the agglomeration of nanocrystalline material.[43,44] We continued investigating the effects of the addition amount of dilute ammonia solution (Table S2). When 15 μL of dilute ammonia solution was introduced, a nanochain structure which was composed of large nanoparticles with irregular edges appeared, but the products were still slightly agglomerated (Figure S4B). Interestingly, uniform nanochain networks were formed when 150 μL of dilute ammonia solution was added into the reaction system (Figure S4C). With a further increase of the ammonia solution up to 500 μL, semblable morphology was obtained except that the surface of the nanochain becomes smoother (Figure S4D). These results reveal that ammonia plays a vital role in the process of the synthetic reaction.

In this research, ammonia acts as a complexant first to form the coordination ion of $Cu(NH_3)_4^{2+}$ and $Pt(NH_3)_nCl_m^{4-m}$ ($n + m = 6$); the change of the metal precursors would diminish the reduction potential of metal ions. By using an ice bath, the nucleation and growth rates could be decreased from two aspects, which could avoid producing smaller aggregated nanoparticles.[51,52] As shown in Figure S5, heterogeneous aggregated nanocrystals appeared when the reaction proceeded at room temperature. In this reaction system, the Pt−Cu nucleus is first generated via co-reduction with hydrazine, and then NH_3 molecules are selectively adsorbed onto the specific crystal planes promptly to decrease surface energy and prevent their anisotropic growth. The deposition of the newly formed metal atoms preferentially occurs on the (111) planes, thus facilitating the growth along the (111) directions.[53,54] Therefore, NH_3 can act as a structure-directing agent to control the morphology of nanocrystalline material.

To shed light on the structural evolution of the nanomaterials, the intermediates were tracked through the time-dependent TEM experiments (Figure S6). During the initial period of reaction, small nanoparticles were formed; with the accumulating of the reaction time, the nanochain networks were generated. About 5 min later, well-defined nanochain networks began to evolve, and no obvious difference was found even after the prolonged reaction time. All of these facts demonstrate the rapid and simple synthetic process of 3D p-PtCu NCNs. During the reaction, self-assembly of PtCu nanocrystalline occurs simultaneously due to the oriented attachment. The formation of porous nanochain networks can be ascribed to the synergistic effect of van der Waals' forces and hydrogen-bonding interaction. Both of the two intermolecular forces promote the oriented attachment of PtCu nanocrystalline together via Ostwald ripening, resulting in the fusion of the nanoparticles.[43,55,56] Figure 4 briefly describes the formation mechanism of 3D p-PtCu NCNs.

Subsequently, the electrocatalytic performances of 3D p-Pt_xCu_{100-x} NCNs were investigated by cyclic voltammetry

DOI: 10.1021/acssuschemeng.7b03047
ACS Sustainable Chem. Eng. 2017, 5, 11086−11095

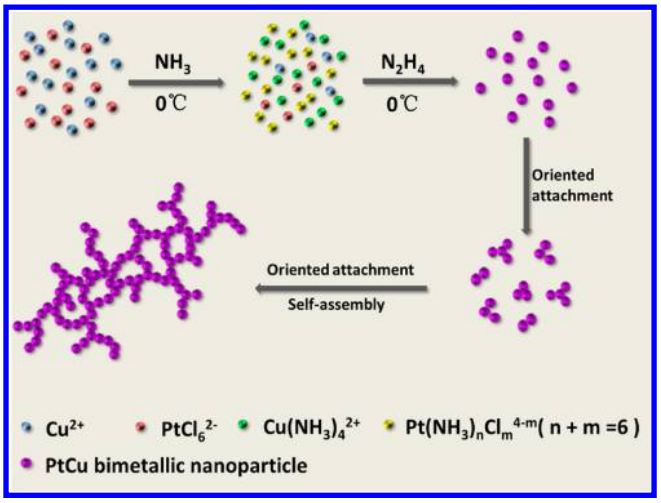

Figure 4. Schematic diagram of the formation mechanism of 3D p-PtCu NCNs.

(CV) experiments. Before the test, the modified GCE was activated by cyclic scanning electrode between −0.2 and 1.0 V (vs Ag/AgCl) in 0.5 M H_2SO_4 until typical stable Pt-like CV profiles are obtained. Figure S7A demonstrates the changes in the shapes of CVs for 3D p-$Pt_{46}Cu_{54}$ NCNs with increasing cycles in 0.5 M H_2SO_4 electrolyte at ambient temperature. Electrochemical dealloying may happen in the process, which has been proposed to be a valid strategy to obtain electrocatalysts with high performance.[42,49,57,58] It shows that the first cycle and second cycle CV curves display smaller hydrogen desorption peaks (−0.2 to 0.1 V), implying the complete surface segregation of Cu in PtCu alloys.[39,49,57] Furthermore, a distinct faradaic current peak at 0.35 V probably corresponds to the dissolution of Cu.[49] The Cu dissolution peak gradually decreases with the increase of CV cycles, while the hydrogen desorption peak is increasingly obvious. After the 15th cycles, the peak of Cu dissolution disappears completely, generating a typical Pt-like CV profile. Negligible change happens in the subsequent CV cycle profiles. The structure and composition of 3D p-$Pt_{46}Cu_{54}$ NCNs have been analyzed after electrochemical activation. As shown in Figure S8A,B, the nanostructure of 3D p-$Pt_{46}Cu_{54}$ NCNs changed to some extent after the electrochemical activation. This change was caused by the dissolution of Cu in the materials probably. On the basis of the EDS analysis (Figure S8C), the content of Cu decreased distinctly after the activation. This phenomenon revealed that the active Pt−Cu catalysts were actually obtained through the dealloying process.[39,59] Selective dissolution of Cu took place during the electrochemical activation process that would endow 3D p-$Pt_{46}Cu_{54}$ NCNs with some favorable characteristics, such as the exposure of active sites and atomic rearrangement of Pt at surfaces which are desirable for their electrocatalytic activity.[59,60]

Figure S7B shows corresponding stable CV curves of different 3D p-Pt_xCu_{100-x} NCNs and commercial Pt/C in 0.5 M H_2SO_4 electrolyte at a scan rate of 100 mV s^{-1}. All catalysts exhibit typical hydrogen adsorption/desorption peaks with one accord. The CV curves were further used to evaluate the electrochemically active surface areas (ECSA) for all electrocatalysts (eq S1).[43] The ECSA data for these materials are measured as follows: 29.59 m^2 g_{Pt}^{-1} for $Pt_{63}Cu_{37}$, 31.39 m^2 g_{Pt}^{-1} for $Pt_{46}Cu_{54}$, 38.59 m^2 g_{Pt}^{-1} for $Pt_{34}Cu_{66}$, 42.74 m^2 g_{Pt}^{-1} for $Pt_{29}Cu_{71}$, and 69.55 m^2 g_{Pt}^{-1} for commercial Pt/C.

The catalytic properties of 3D p-Pt_xCu_{100-x} NCNs and commercial Pt/C toward EG electrooxidation are tested by CV measurement. Figure 5A exhibits the CV curves of p-Pt_xCu_{100-x}

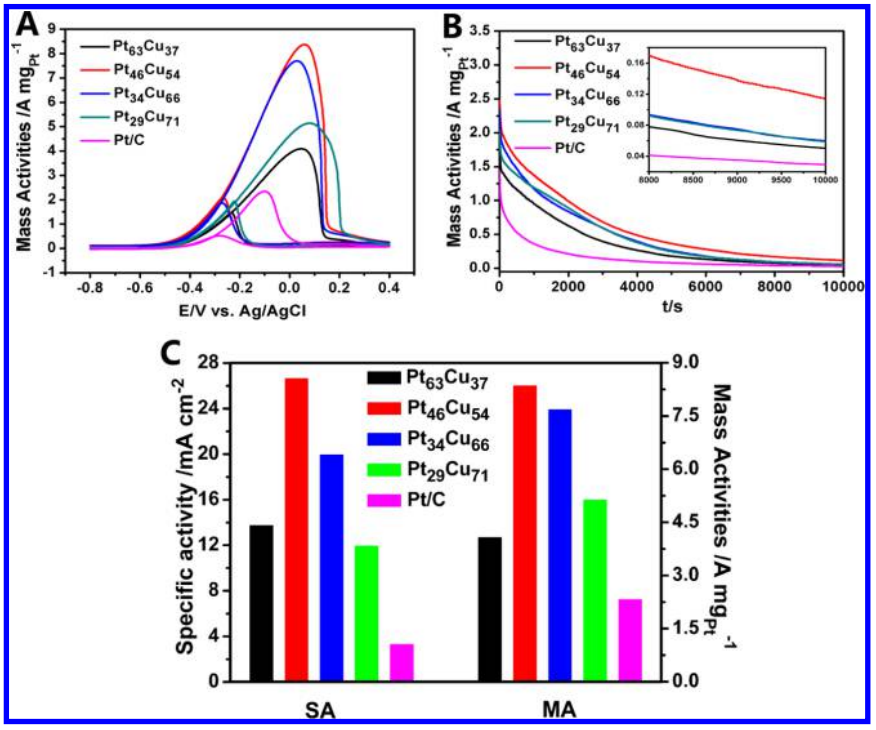

Figure 5. (A) CV curves of as-prepared 3D p-Pt_xCu_{100-x} NCNs and commercial Pt/C in 0.5 M EG + 0.5 M NaOH electrolyte with a scan rate of 50 mV s^{-1}. (B) Current−time curves recorded at −0.2 V (the inset is the amplifying image of the eventual test regions). (C) Specific and mass activities of 3D p-Pt_xCu_{100-x} NCNs and Pt/C for EGOR.

DOI: 10.1021/acssuschemeng.7b03047
ACS Sustainable Chem. Eng. 2017, 5, 11086−11095

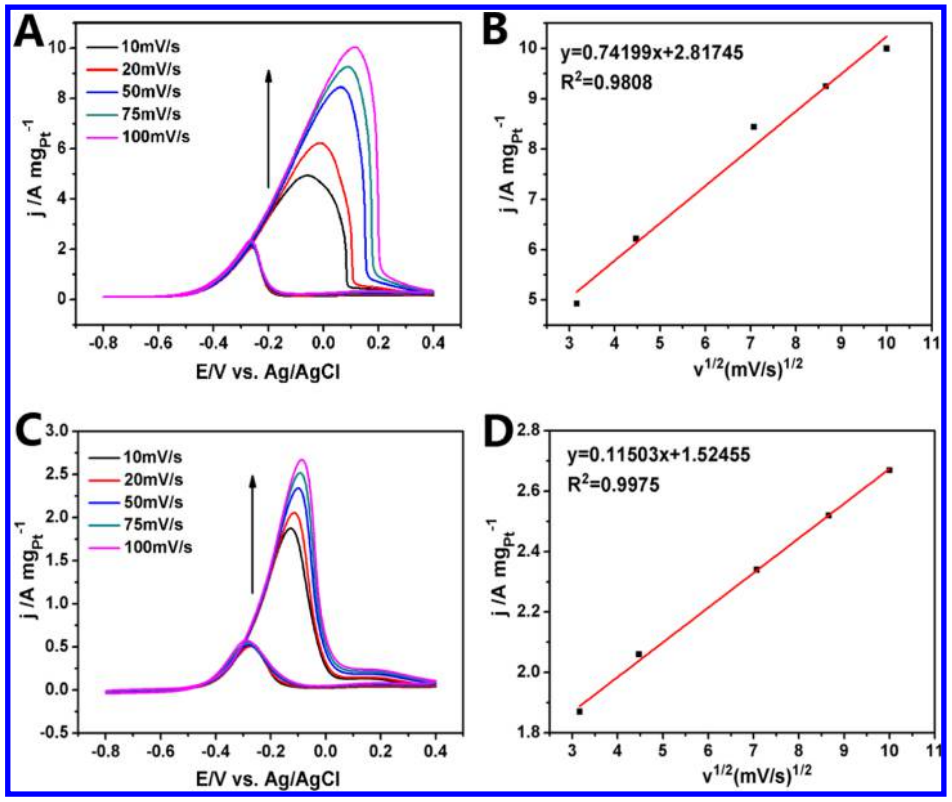

Figure 6. (A) CV of EGOR on the 3D p-$Pt_{46}Cu_{54}$ NCNs at different scan rates and (B) the corresponding plot of j_p versus $v^{1/2}$. (C) CV of EGOR on commercial Pt/C at different scan rates and (D) the corresponding plot of j_p versus $v^{1/2}$.

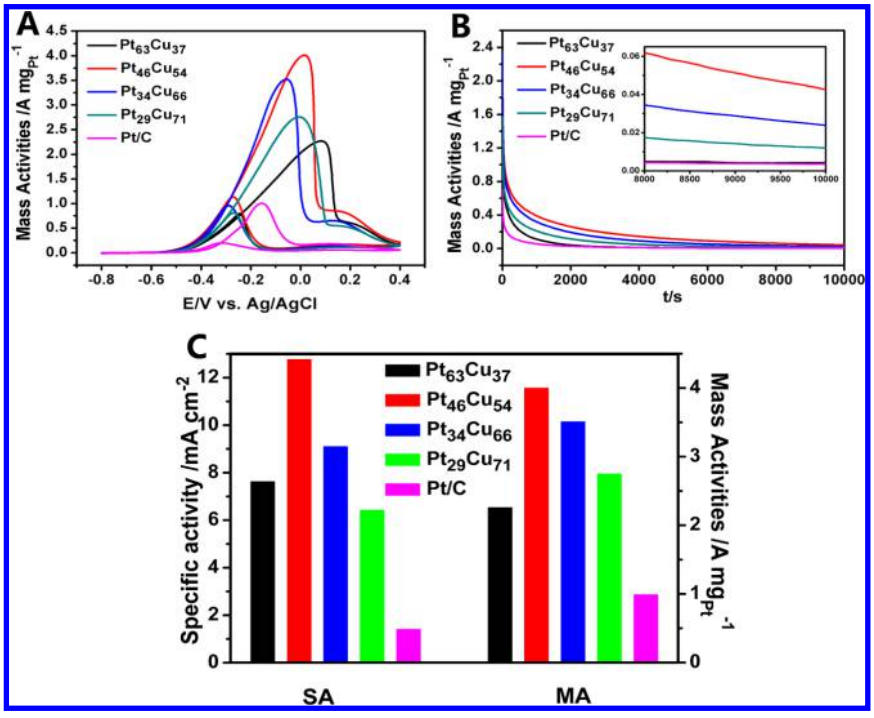

Figure 7. (A) CV curves of as-prepared 3D p-Pt_xCu_{100-x} NCNs and commercial Pt/C in 0.5 M glycerol + 0.5 M NaOH electrolyte with a scan rate of 50 mV s^{-1}. (B) Current−time curves recorded at −0.2 V (the inset is the amplifying image of the eventual test regions). (C) Specific and mass activities of 3D p-Pt_xCu_{100-x} NCNs and Pt/C for GOR.

NCNs and commercial Pt/C in 0.5 M EG + 0.5 M NaOH at a scan rate of 50 mV s^{-1}. It should be pointed out that there are two diverse peaks during the scanning process. In the forward scan, the peaks are derived from EG oxidation; in the backward scan, the emergence of the peaks is bound up with the elimination of carbonaceous species (such as CO) generated during the electrooxidation process.[61,62] Obviously, all the prepared 3D p-Pt_xCu_{100-x} NCNs presented higher mass activity

DOI: 10.1021/acssuschemeng.7b03047
ACS Sustainable Chem. Eng. 2017, 5, 11086−11095

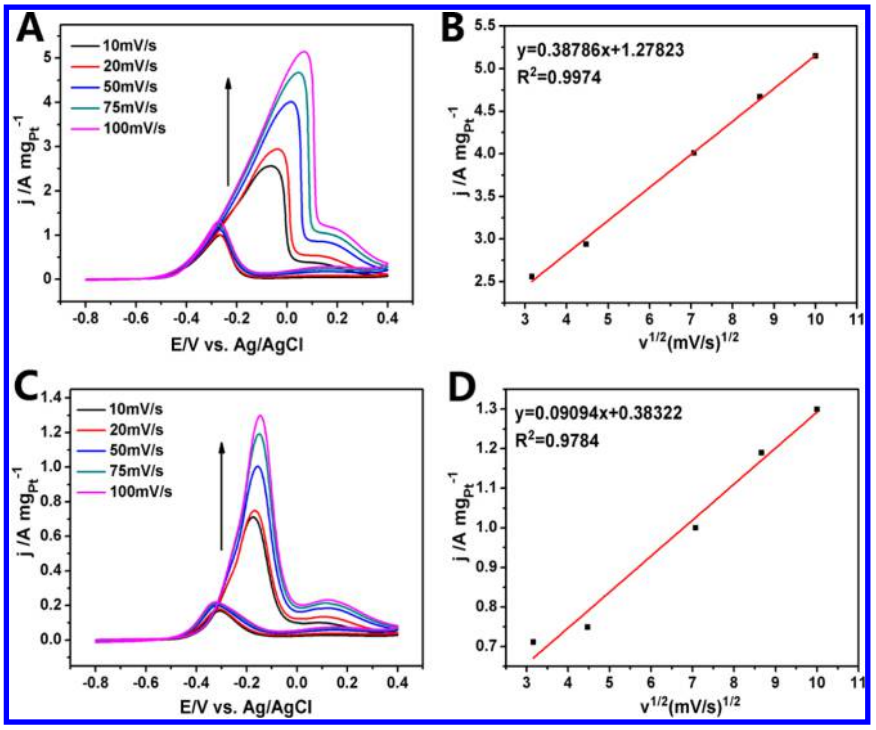

Figure 8. (A) CV of GOR on the 3D p-$Pt_{46}Cu_{54}$ NCNs at different scan rates and (B) the corresponding plot of j_p versus $v^{1/2}$. (C) CV of GOR on commercial Pt/C at different scan rates and (D) the corresponding plot of j_p versus $v^{1/2}$.

than the Pt/C. Furthermore, the p-Pt_xCu_{100-x} NCNs exhibit different catalytic properties as their composition changed, certifying the strong relation between catalytic activity and their composition. Among them, the p-$Pt_{46}Cu_{54}$ NCNs exhibit the highest mass activity of 8.38 A mg_{Pt}^{-1}, and this value is 3.58-fold that of commercial Pt/C (2.34 A mg_{Pt}^{-1}). The specific activity was normalized by the ECSA;[58] the p-$Pt_{46}Cu_{54}$ NCNs present a specific activity of 26.7 mA cm^{-2}, and the value is 7.92-fold that of commercial Pt/C (3.37 mA cm^{-2}). Figure 5C shows mass and specific activities of $Pt_{63}Cu_{37}$, $Pt_{46}Cu_{54}$, $Pt_{34}Cu_{66}$, $Pt_{29}Cu_{71}$, and Pt/C for EG oxidation. All of the prepared p-Pt_xCu_{100-x} NCNs possess an obviously higher activity than the commercial Pt/C, testifying to their outstanding electrocatalytic activity.

The stability of the nanomaterials for EG electrooxidation was investigated by chronoamperometry. Compared with commercial Pt/C, the prepared 3D p-Pt_xCu_{100-x} NCNs all display a slower decline in current density (Figure 5B). After 10 000s of tests, the current densities remaining on these 3D p-Pt_xCu_{100-x} NCNs all remain higher than that of commercial Pt/C. In detail, the $Pt_{63}Cu_{37}$, $Pt_{46}Cu_{54}$, $Pt_{34}Cu_{66}$, and $Pt_{29}Cu_{71}$ could maintain 92.75%, 95.88%, 93%, and 95% of the original activity after the long duration test, respectively, while only 75% of the initial activity could be retained for Pt/C (Figure S9). The above results further confirm the superior activity and stability of 3D p-Pt_xCu_{100-x} NCNs in EG oxidation.

The transport characteristics of EG on different modified electrodes were studied by CV measurements. Figure 6A,C shows the CV profiles of 3D p-$Pt_{46}Cu_{54}$ NCNs and Pt/C for EG electrooxidation at different scan rates, varying from 10 to 100 mV s^{-1}. The peak current density (j_p) rises along with the increasing scan rate, and the j_p potential shows positive shifts successively. As a result, it displays a linear relationship between j_p and the square root of the scan rate ($v^{1/2}$) both for p-$Pt_{46}Cu_{54}$ NCNs and Pt/C (Figure 6B,D). The relationship between $v^{1/2}$ and j_p exists for all the 3D p-Pt_xCu_{100-x} NCNs (Figure S10). The results illustrate that EG oxidation on 3D p-Pt_xCu_{100-x} NCNs and Pt/C all follows a diffusion-controlled process.[4,63,64] Compared with Pt/C, 3D p-Pt_xCu_{100-x} NCNs obtained higher slope values, which implies enhanced electrooxidation kinetics of the porous nanochain networks (eq S2).[4,63,64] This result should be used to explain the high electrocatalytic performance of the 3D p-Pt_xCu_{100-x} NCNs to a certain extent.

The electrocatalytic performance of prepared 3D p-Pt_xCu_{100-x} NCNs for glycerol electrooxidation was further explored. Figure 7A exhibits the CV curves of 3D p-Pt_xCu_{100-x} NCNs and commercial Pt/C in 0.5 M glycerol + 0.5 M NaOH at a scan rate of 50 mV s^{-1}. As illustrated in Figure 7A, the p-$Pt_{46}Cu_{54}$ NCNs also display the highest activity of 4.01 A mg_{Pt}^{-1}, which is 4.01-fold that of Pt/C (1 A mg_{Pt}^{-1}). The electrocatalytic activity conforms to the following order: $Pt_{46}Cu_{54}$ > $Pt_{34}Cu_{66}$ > $Pt_{29}Cu_{71}$ > $Pt_{63}Cu_{37}$ > Pt/C. This is in accordance with the tendency of EG electrooxidation. Figure 7C shows mass and specific activities of $Pt_{63}Cu_{37}$, $Pt_{46}Cu_{54}$, $Pt_{34}Cu_{66}$, $Pt_{29}Cu_{71}$, and Pt/C for glycerol oxidation. The specific activity of 3D p-$Pt_{46}Cu_{54}$ NCNs (12.8 mA cm^{-2}) is 8.89-fold that of Pt/C (1.44 mA cm^{-2}). The stabilities of the electrocatalysts for glycerol electrooxidation were measured by chronoamperometry (Figure 7B). After 10 000s of tests, all the 3D p-Pt_xCu_{100-x} NCNs show higher stability than that of Pt/C. After the long duration test, the $Pt_{63}Cu_{37}$, $Pt_{46}Cu_{54}$, $Pt_{34}Cu_{66}$, and $Pt_{29}Cu_{71}$ could maintain 88.64%, 100%, 99.23%, and 98.29% of the original activity separately, while only 61.53% of the initial activity was retained for Pt/C (Figure S11). These results reveal the superior stability of 3D p-Pt_xCu_{100-x} NCNs in glycerol electrooxidation.

As shown in Figure 8A,C, the j_p also increases as the scan rate increase, and the j_p potential shifts positively for both p-$Pt_{46}Cu_{54}$ NCNs and Pt/C catalyst. A linear relationship is also found between j_p and $v^{1/2}$ in the GOR (Figure 8B,D). The

DOI: 10.1021/acssuschemeng.7b03047
ACS Sustainable Chem. Eng. 2017, 5, 11086−11095

linear relationship was also established for other 3D p-Pt_xCu_{100-x} NCNs (Figure S12). The slope values for the 3D p-Pt_xCu_{100-x} NCNs are all bigger than that of commercial Pt/C. The results indicate the intensive electrooxidation kinetics of the 3D p-Pt_xCu_{100-x} NCNs, which are ascribed to the improvement of their electrocatalytic performance.

Table S3 displays all electrochemical parameters of 3D p-Pt_xCu_{100-x} NCNs and commercial Pt/C. The mass activities for EGOR and GOR of 3D p-Pt_xCu_{100-x} NCNs were compared with other materials and listed in Table S4, which further reveal that the prepared 3D p-Pt_xCu_{100-x} NCNs exhibit a high catalytic performance for EGOR and GOR. The following factors are bound up with the enhanced electrocatalytic activities of 3D p-Pt_xCu_{100-x} NCNs: (1) The special 3D nanostructures owns large surface area and abundant active sites via the high porosity, which efficiently improves the surface mass transport and gas diffusion.[21,35,36] In addition, as self-supported catalysts, they possess intensive durability as the carbon support-corrosion is eliminated.[17,38] (2) The variational electronic states of the active component Pt in Pt-based alloys may promote their catalytic properties.[4,5] Moreover, the lattice-mismatch strain between Pt and the second metal could arouse the downshift of the d-band center, which could decrease the chemisorption between Pt and the oxygenated species, and thus improve their electrocatalytic activity.[21,32,42] (3) Electrochemical dealloying is supposed to make a contribution to the excellent performance of 3D p-Pt_xCu_{100-x} NCNs. In the electrochemical activation process, selective dissolution of Cu would endow 3D p-Pt_xCu_{100-x} NCNs with some advantageous characteristics such as the exposure of active sites and atomic rearrangement of Pt at the surface which are desirable for their electrocatalytic activity.[39,59,60]

CONCLUSIONS

To sum up, we have successfully developed an effective one-pot strategy to synthesize bimetallic alloyed 3D p-Pt_xCu_{100-x} NCNs with tunable compositions, wherein ammonia acted as the structure-directing reagent and hydrazine hydrate as the reducing reagent. The prepared nanomaterials exhibited prominent catalytic activity and stability for EGOR and GOR in alkaline solution compared with commercial Pt/C, in particular, 3D p-$Pt_{46}Cu_{54}$ NCNs possess the best mass activity of 8.38 A mg_{Pt}^{-1} for EGOR and 4.01 A mg_{Pt}^{-1} for GOR, which are 3.58-fold and 4.01-fold that of commercial Pt/C, respectively. The outstanding performance could be closely related to the typical 3D porous nanostructures, synergism between Pt and Cu, and the electrochemical dealloying. The synthetic strategy could be expected to synthesize promising 3D porous Pt-based nanomaterials for the development of direct fuel cells.

ASSOCIATED CONTENT

Supporting Information

The Supporting Information is available free of charge on the ACS Publications website at DOI: 10.1021/acssuschemeng.7b03047.

Additional characterization data, including EDS, SEM, TEM, and CV; data tables; and equation information (PDF)

AUTHOR INFORMATION

Corresponding Author

*E-mail: hyhan@mail.hzau.edu.cn.

ORCID

Heyou Han: 0000-0001-9406-0722

Notes

The authors declare no competing financial interest.

ACKNOWLEDGMENTS

We acknowledge the financial support from National Key R & D Program (2016YFD0500700), the National Natural Science Foundation of China (21375043 and 21778020), and the Fundamental Research Funds for the Central Universities (2662015QD026).

REFERENCES

(1) Chu, S.; Majumdar, A. Opportunities and Challenges for a Sustainable Energy Future. *Nature* **2012**, *488*, 294−303.

(2) You, H.; Yang, S.; Ding, B.; Yang, H. Synthesis of Colloidal Metal and Metal Alloy Nanoparticles for Electrochemical Energy Applications. *Chem. Soc. Rev.* **2013**, *42*, 2880−2904.

(3) Peng, Z.; Yang, H. Designer Platinum Nanoparticles: Control of Shape, Composition in Alloy, Nanostructure and Electrocatalytic Property. *Nano Today* **2009**, *4*, 143−164.

(4) Hong, W.; Shang, C.; Wang, J.; Wang, E. Bimetallic PdPt Nanowire Networks with Enhanced Electrocatalytic Activity for Ethylene Glycol and Glycerol Oxidation. *Energy Environ. Sci.* **2015**, *8*, 2910−2915.

(5) Li, S.; Lai, J.; Luque, R.; Xu, G. Designed Multimetallic Pd Nanosponges with Enhanced Electrocatalytic Activity for Ethylene Glycol and Glycerol Oxidation. *Energy Environ. Sci.* **2016**, *9*, 3097−3102.

(6) Serov, A.; Kwak, C. Recent Achievements in Direct Ethylene Glycol Fuel Cells (DEGFC). *Appl. Catal., B* **2010**, *97*, 1−12.

(7) Villa, A.; Dimitratos, N.; Chan-Thaw, C. E.; Hammond, C.; Prati, L.; Hutchings, G. J. Glycerol Oxidation Using Gold-Containing Catalysts. *Acc. Chem. Res.* **2015**, *48*, 1403−1412.

(8) Falase, A.; Main, M.; Garcia, K.; Serov, A.; Lau, C.; Atanassov, P. Electrooxidation of Ethylene Glycol and Glycerol by Platinum-Based Binary and Ternary Nano-structured Catalysts. *Electrochim. Acta* **2012**, *66*, 295−301.

(9) Zalineeva, A.; Serov, A.; Padilla, M.; Martinez, U.; Artyushkova, K.; Baranton, S.; Coutanceau, C.; Atanassov, P. B. Self-Supported Pd_xBi Catalysts for the Electrooxidation of Glycerol in Alkaline Media. *J. Am. Chem. Soc.* **2014**, *136*, 3937−3945.

(10) Zhang, N.; Feng, Y.; Zhu, X.; Guo, S.; Guo, J.; Huang, X. Superior Bifunctional Liquid Fuel Oxidation and Oxygen Reduction Electrocatalysis Enabled by PtNiPd Core-Shell Nanowires. *Adv. Mater.* **2017**, *29*, 1603774.

(11) Jiang, K.; Wang, P.; Guo, S.; Zhang, X.; Shen, X.; Lu, G.; Su, D.; Huang, X. Ordered PdCu-Based Nanoparticles as Bifunctional Oxygen Reduction and Ethanol-Oxidation Electrocatalysts. *Angew. Chem., Int. Ed.* **2016**, *55*, 9030−9035.

(12) Wu, J.; Yang, H. Platinum-Based Oxygen Reduction Electrocatalysts. *Acc. Chem. Res.* **2013**, *46* (8), 1848−1857.

(13) Huang, X.; Zhao, Z.; Cao, L.; Chen, Y.; Zhu, E.; Lin, Z.; Li, M.; Yan, A.; Zettl, A.; Wang, Y. M.; Duan, X.; Mueller, T.; Huang, Y. High-Performance Transition Metal-Doped Pt_3Ni Octahedra for Oxygen Reduction Reaction. *Science* **2015**, *348*, 1230−1234.

(14) Zhang, H.; Jin, M.; Xia, Y. Enhancing the Catalytic and Electrocatalytic Properties of Pt-Based Catalysts by Forming Bimetallic Nanocrystals with Pd. *Chem. Soc. Rev.* **2012**, *41*, 8035−8049.

(15) Porter, N. S.; Wu, H.; Quan, Z.; Fang, J. Shape-Control and Electrocatalytic Activity-Enhancement of Pt-Based Bimetallic Nanocrystals. *Acc. Chem. Res.* **2013**, *46* (8), 1867−1877.

DOI: 10.1021/acssuschemeng.7b03047
ACS Sustainable Chem. Eng. 2017, 5, 11086−11095

(16) Debe, M. K. Electrocatalyst Approaches and Challenges for Automotive Fuel Cells. *Nature* **2012**, *486*, 43−51.
(17) Tamaki, T.; Kuroki, H.; Ogura, S.; Fuchigami, T.; Kitamoto, Y.; Yamaguchi, T. Connected Nanoparticle Catalysts Possessing a Porous, Hollow Capsule Structure as Carbon-Free Electrocatalysts for Oxygen Reduction in Polymer Electrolyte Fuel Cells. *Energy Environ. Sci.* **2015**, *8*, 3545−3549.
(18) Gan, L.; Heggen, M.; O'Malley, R.; Theobald, B.; Strasser, P. Understanding and Controlling Nanoporosity Formation for Improving the Stability of Bimetallic Fuel Cell Catalysts. *Nano Lett.* **2013**, *13*, 1131−1138.
(19) Luo, S.; Shen, P. K. Concave Platinum−Copper Octopod Nanoframes Bounded with Multiple High Index Facets for Efficient Electrooxidation Catalysis. *ACS Nano* **2016**, DOI: 10.1021/acsnano.6b04458.
(20) Fu, G.-T.; Xia, B.-Y.; Ma, R.-G.; Chen, Y.; Tang, Y.-W.; Lee, J.-M. Trimetallic PtAgCu@PtCu Core@Shell Concave Nanooctahedrons with Enhanced Activity for Formic Acid Oxidation Reaction. *Nano Energy* **2015**, *12*, 824−832.
(21) Fu, S.; Zhu, C.; Du, D.; Lin, Y. Enhanced Electrocatalytic Activities of PtCuCoNi Three-Dimensional Nanoporous Quaternary Alloys for Oxygen Reduction and Methanol Oxidation Reactions. *ACS Appl. Mater. Interfaces* **2016**, *8*, 6110−6116.
(22) Gilroy, K. D.; Ruditskiy, A.; Peng, H.-C.; Qin, D.; Xia, Y. Bimetallic Nanocrystals: Syntheses, Properties, and Applications. *Chem. Rev.* **2016**, *116*, 10414−10472.
(23) Liu, X.; Wang, D.; Li, Y. Synthesis and Catalytic Properties of Bimetallic Nanomaterials with Various Architectures. *Nano Today* **2012**, *7*, 448−466.
(24) Sun, X.; Li, D.; Ding, Y.; Zhu, W.; Guo, S.; Wang, Z. L.; Sun, S. Core/Shell Au/CuPt Nanoparticles and Their Dual Electrocatalysis for Both Reduction and Oxidation Reactions. *J. Am. Chem. Soc.* **2014**, *136*, 5745−5749.
(25) Lim, B.; Jiang, M.; Camargo, P. H. C.; Cho, E. C.; Tao, J.; Lu, X.; Zhu, Y.; Xia, Y. Pd-Pt Bimetallic Nanodendrites with High Activity for Oxygen Reduction. *Science* **2009**, *324*, 1302−1305.
(26) Ud Din, M. A.; Saleem, F.; Ni, B.; Yong, Y.; Wang, X. Porous Tetrametallic PtCuBiMn Nanosheets with a High Catalytic Activity and Methanol Tolerance Limit for Oxygen Reduction Reactions. *Adv. Mater.* **2017**, *29*, 1604994.
(27) Zhang, L.; Roling, L. T.; Wang, X.; Vara, M.; Chi, M.; Liu, J.; Choi, S.; Park, J.; Herron, J. A.; Xie, Z.; Mavrikakis, M.; Xia, Y. Platinum-Based Nanocages with Subnanometer-Thick Walls and Well-Defined, Controllable Facets. *Science* **2015**, *349*, 412−416.
(28) Bu, L.; Guo, S.; Zhang, X.; Shen, X.; Su, D.; Lu, G.; Zhu, X.; Yao, J.; Guo, J.; Huang, X. Surface Engineering of Hierarchical Platinum-Cobalt Nanowires for Efficient Electrocatalysis. *Nat. Commun.* **2016**, *7*, 11850.
(29) Zhang, N.; Bu, L.; Guo, S.; Guo, J.; Huang, X. Screw Thread-Like Platinum-Copper Nanowires Bounded with High-Index Facets for Efficient Electrocatalysis. *Nano Lett.* **2016**, *16*, 5037−5043.
(30) Zhu, H.; Wu, Z.; Su, D.; Veith, G. M.; Lu, H.; Zhang, P.; Chai, S.-H.; Dai, S. Constructing Hierarchical Interfaces: TiO_2-Supported PtFe-FeO_x Nanowires for Room Temperature CO Oxidation. *J. Am. Chem. Soc.* **2015**, *137*, 10156−10159.
(31) Chen, C.; Kang, Y.; Huo, Z.; Zhu, Z.; Huang, W.; Xin, H. L.; Snyder, J. D.; Li, D.; Herron, J. A.; Mavrikakis, M.; Chi, M.; More, K. L.; Li, Y.; Markovic, N. M.; Somorjai, G. A.; Yang, P.; Stamenkovic, V. R. Highly Crystalline Multimetallic Nanoframes with Three-Dimensional Electrocatalytic Surfaces. *Science* **2014**, *343*, 1339−1343.
(32) Zhang, Z.; Luo, Z.; Chen, B.; Wei, C.; Zhao, J.; Chen, J.; Zhang, X.; Lai, Z.; Fan, Z.; Tan, C.; Zhao, M.; Lu, Q.; Li, B.; Zong, Y.; Yan, C.; Wang, G.; Xu, Z. J.; Zhang, H. One-Pot Synthesis of Highly Anisotropic Five-Fold-Twinned PtCu Nanoframes Used as a Bifunctional Electrocatalyst for Oxygen Reduction and Methanol Oxidation. *Adv. Mater.* **2016**, *28*, 8712−8717.
(33) Chen, S.; Su, H.; Wang, Y.; Wu, W.; Zeng, J. Size-Controlled Synthesis of Platinum-Copper Hierarchical Trigonal Bipyramid Nanoframes. *Angew. Chem., Int. Ed.* **2015**, *54*, 108−113.
(34) Luo, S.; Tang, M.; Shen, P. K.; Ye, S. Atomic-Scale Preparation of Octopod Nanoframes with High-Index Facets as Highly Active and Stable Catalysts. *Adv. Mater.* **2017**, *29*, 1601687.
(35) Zhu, C.; Du, D.; Eychmüller, A.; Lin, Y. Engineering Ordered and Nonordered Porous Noble Metal Nanostructures: Synthesis, Assembly, and Their Applications in Electrochemistry. *Chem. Rev.* **2015**, *115*, 8896−8943.
(36) Zhu, C.; Shi, Q.; Fu, S.; Song, J.; Xia, H.; Du, D.; Lin, Y. Efficient Synthesis of MCu (M = Pd, Pt, and Au) Aerogels with Accelerated Gelation Kinetics and their High Electrocatalytic Activity. *Adv. Mater.* **2016**, *28*, 8779−8783.
(37) Liu, J.; Huang, Z.; Cai, K.; Zhang, H.; Lu, Z.; Li, T.; Zuo, Y.; Han, H. Clean Synthesis of an Economical 3D Nanochain Network of PdCu Alloy with Enhanced Electrocatalytic Performance towards Ethanol Oxidation. *Chem. - Eur. J.* **2015**, *21*, 17779−17785.
(38) Liu, W.; Herrmann, A.-K.; Bigall, N. C.; Rodriguez, P.; Wen, D.; Oezaslan, M.; Schmidt, T. J.; Gaponik, N.; Eychmüller, A. Noble Metal Aerogels-Synthesis, Characterization, and Application as Electrocatalysts. *Acc. Chem. Res.* **2015**, *48*, 154−162.
(39) Xia, B. Y.; Wu, H. B.; Wang, X.; Lou, X. W. One-Pot Synthesis of Cubic $PtCu_3$ Nanocages with Enhanced Electrocatalytic Activity for the Methanol Oxidation Reaction. *J. Am. Chem. Soc.* **2012**, *134*, 13934−13937.
(40) Jia, Y.; Jiang, Y.; Zhang, J.; Zhang, L.; Chen, Q.; Xie, Z.; Zheng, L. Unique Excavated Rhombic Dodecahedral $PtCu_3$ Alloy Nanocrystals Constructed with Ultrathin Nanosheets of High-Energy {110} Facets. *J. Am. Chem. Soc.* **2014**, *136*, 3748−3751.
(41) Cao, X.; Wang, N.; Han, Y.; Gao, C.; Xu, Y.; Li, M.; Shao, Y. PtAg Bimetallic Nanowires: Facile Synthesis and Their Use as Excellent Electrocatalysts Toward Low-Cost Fuel Cells. *Nano Energy* **2015**, *12*, 105−114.
(42) Strasser, P.; Koh, S.; Anniyev, T.; Greeley, J.; More, K.; Yu, C.; Liu, Z.; Kaya, S.; Nordlund, D.; Ogasawara, H.; Toney, M. F.; Nilsson, A. Lattice-Strain Control of the Activity in Dealloyed Core-Shell Fuel Cell Catalysts. *Nat. Chem.* **2010**, *2*, 454−460.
(43) He, L.-L.; Zheng, J.-N.; Song, P.; Zhong, S.-X.; Wang, A.-J.; Chen, Z.; Feng, J.-J. Facile Synthesis of Platinum-Gold Alloyed String-Bead Nanochain Networks with the Assistance of Allantoin and Their Enhanced Electrocatalytic Performance for Oxygen Reduction and Methanol Oxidation Reactions. *J. Power Sources* **2015**, *276*, 357−364.
(44) He, L.-L.; Song, P.; Wang, A.-J.; Zheng, J.-N.; Mei, L.-P.; Feng, J.-J. A General Strategy for the Facile Synthesis of AuM (M = Pt/Pd) Alloyed Flowerlike-Assembly Nanochains for Enhanced Oxygen Reduction Reaction. *J. Mater. Chem. A* **2015**, *3*, 5352−5359.
(45) Wu, L.; Yin, W.; Tang, K.; Li, D.; Shao, K.; Zuo, Y.; Ma, J.; Liu, J.; Han, H. Enzymatic Biosensor of Horseradish Peroxidase Immobilized on Au-Pt Nanotube/Au-Graphene for the Simultaneous Determination of Antioxidants. *Anal. Chim. Acta* **2016**, *933*, 89−96.
(46) Kariuki, N. N.; Cansizoglu, M. F.; Begum, M.; Yurukcu, M.; Yurtsever, F. M.; Karabacak, T.; Myers, D. J. SAD−GLAD Pt−Ni@Ni Nanorods as Highly Active Oxygen Reduction Reaction Electrocatalysts. *ACS Catal.* **2016**, *6*, 3478−3485.
(47) Xia, B. Y.; Wu, H. B.; Li, N.; Yan, Y.; Lou, X. W.; Wang, X. One-Pot Synthesis of Pt-Co Alloy Nanowire Assemblies with Tunable Composition and Enhanced Electrocatalytic Properties. *Angew. Chem., Int. Ed.* **2015**, *54*, 3797−3801.
(48) Choi, D. S.; Robertson, A. W.; Warner, J. H.; Kim, S. O.; Kim, H. Low-Temperature Chemical Vapor Deposition Synthesis of Pt-Co Alloyed Nanoparticles with Enhanced Oxygen Reduction Reaction Catalysis. *Adv. Mater.* **2016**, *28*, 7115−7122.
(49) Nosheen, F.; Zhang, Z.; Zhuang, J.; Wang, X. One-Pot Fabrication of Single-Crystalline Octahedral Pt-Cu Nanoframes and Their Enhanced Electrocatalytic Activity. *Nanoscale* **2013**, *5*, 3660−3663.
(50) Zuo, Y.; Li, T.; Ren, H.; Zhu, G.; Han, K.; Zhuang, L.; Han, H. Self-Assembly of Pt-Based Truncated Octahedral Crystals into Metal-Frameworks towards Enhanced Electrocatalytic Activity. *J. Mater. Chem. A* **2016**, *4*, 15169−15180.

DOI: 10.1021/acssuschemeng.7b03047
ACS Sustainable Chem. Eng. 2017, 5, 11086−11095

(51) Wang, W.; Wang, D.; Liu, X.; Peng, Q.; Li, Y. Pt-Ni Nanodendrites with High Hydrogenation Activity. *Chem. Commun.* **2013**, *49*, 2903−2905.
(52) Wang, F.; Li, C.; Sun, L.-D.; Xu, C.-H.; Wang, J.; Yu, J. C.; Yan, C.-H. Porous Single-Crystalline Palladium Nanoparticles with High Catalytic Activities. *Angew. Chem., Int. Ed.* **2012**, *51*, 4872−4876.
(53) Liu, P.; Qin, R.; Fu, G.; Zheng, N. Surface Coordination Chemistry of Metal Nanomaterials. *J. Am. Chem. Soc.* **2017**, *139*, 2122−2131.
(54) Dai, Y.; Mu, X.; Tan, Y.; Lin, K.; Yang, Z.; Zheng, N.; Fu, G. Carbon Monoxide-Assisted Synthesis of Single-Crystalline Pd Tetrapod Nanocrystals through Hydride Formation. *J. Am. Chem. Soc.* **2012**, *134*, 7073−7080.
(55) Zhang, Q.-L.; Ju, K.-J.; Huang, X.-Y.; Wang, A.-J.; Wei, J.; Feng, J.-J. Metformin Mediated Facile Synthesis of AuPt Alloyed Nanochains with Enhanced Electrocatalytic Properties for Alcohol Oxidation. *Electrochim. Acta* **2015**, *182*, 305−311.
(56) Tang, Z.; Kotov, N. A.; Giersig, M. Spontaneous Organization of Single CdTe Nanoparticles into Luminescent Nanowires. *Science* **2002**, *297*, 237−240.
(57) Oezaslan, M.; Heggen, M.; Strasser, P. Size-Dependent Morphology of Dealloyed Bimetallic Catalysts: Linking the Nano to the Macro Scale. *J. Am. Chem. Soc.* **2012**, *134*, 514−524.
(58) Li, M.; Zhao, Z.; Cheng, T.; Fortunelli, A.; Chen, C.-Y.; Yu, R.; Zhang, Q.; Gu, L.; Merinov, B.; Lin, Z.; Zhu, E.; Yu, T.; Jia, Q.; Guo, J.; Zhang, L.; Goddard, W. A., III; Huang, Y.; Duan, X. Ultrafine Jagged Platinum Nanowires Enable Ultrahigh Mass Activity for the Oxygen Reduction Reaction. *Science* **2016**, *354*, 1414−1419.
(59) Koh, S.; Strasser, P. Electrocatalysis on Bimetallic Surfaces: Modifying Catalytic Reactivity for Oxygen Reduction by Voltammetric Surface Dealloying. *J. Am. Chem. Soc.* **2007**, *129*, 12624−12625.
(60) Srivastava, R.; Mani, P.; Hahn, N.; Strasser, P. Efficient Oxygen Reduction Fuel Cell Electrocatalysis on Voltammetrically Dealloyed Pt-Cu-Co Nanoparticles. *Angew. Chem., Int. Ed.* **2007**, *46*, 8988−8991.
(61) Kim, H. J.; Choi, S. M.; Green, S.; Tompsett, G. A.; Lee, S. H.; Huber, G. W.; Kim, W. B. Highly Active and Stable PtRuSn/C Catalyst for Electrooxidations of Ethylene Glycol and Glycerol. *Appl. Catal., B* **2011**, *101*, 366−375.
(62) Li, S.-S.; Hu, Y.-Y.; Feng, J.-J.; Lv, Z.-Y.; Chen, J.-R.; Wang, A.-J. Rapid Room-Temperature Synthesis of Pd Nanodendrites on Reduced Graphene Oxide for Catalytic Oxidation of Ethylene Glycol and Glycerol. *Int. J. Hydrogen Energy* **2014**, *39*, 3730−3738.
(63) Chen, M.; Meng, Y.; Zhou, J.; Diao, G. Platinum Nanoworms Self-Assemble on b -Cyclodextrin Polymer Inclusion Complexes Functionalized Reduced Graphene Oxide as Enhanced Catalyst for Direct Methanol Fuel Cells. *J. Power Sources* **2014**, *265*, 110−117.
(64) Huang, L.; Han, Y.; Zhang, X.; Fang, Y.; Dong, S. One-Step Synthesis of Ultrathin Pt_xPb Nerve-Like Nanowires as Robust Catalysts for Enhanced Methanol Electrooxidation. *Nanoscale* **2017**, *9*, 201−207.

DOI: 10.1021/acssuschemeng.7b03047
ACS Sustainable Chem. Eng. 2017, 5, 11086−11095